



Enhanced reductive debromination and subsequent oxidative ring-opening of decabromodiphenyl ether by integrated catalyst of nZVI supported on magnetic Fe_3O_4 nanoparticles



Lei Tan ^{a,b}, Shaoyou Lu ^c, Zhanqiang Fang ^{a,b,*}, Wen Cheng ^{a,b}, Eric Pokeung Tsang ^{b,d}

^a School of Chemistry and Environment, South China Normal University, Guangzhou 51006, China

^b Guangdong Technology Research Centre for Ecological Management and Remediation of Water System, Guangzhou 51006, China

^c Shenzhen Center for Disease Control and Prevention, Shenzhen 518055, China

^d Department of Science and Environmental Studies, Hong Kong Institute of Education, Hong Kong 00852, China

ARTICLE INFO

Article history:

Received 7 March 2016

Received in revised form 17 June 2016

Accepted 4 July 2016

Available online 5 July 2016

Keywords:

Decabromodiphenyl ether (BDE209)

$\text{Fe}^0@\text{Fe}_3\text{O}_4$ nanoparticles

Ring-opening

Two stage

Mechanism

ABSTRACT

The magnetic $\text{Fe}^0@\text{Fe}_3\text{O}_4$ nanocomposite was prepared and used to achieve the reductive/subsequent oxidative ring-opening of decabromodiphenyl ether (BDE209) in this work. The characterization results indicated that the structure of the composite consisted of small nanoscale zero-valent iron (nZVI) particles surrounding the surface of Fe_3O_4 nanoparticle (NP). A 100% removal efficiency and 80% degradation efficiency of BDE209 was reached by the composite accompanied with ultrasound (called NP/US system) for 36 h, which is higher than that obtained with conventional nZVI particles. Furthermore, the enhanced debromination and ring-opening of BDE209 was realized by a Fenton-like degradation process lasting for 12 h after the addition of H_2O_2 to the NP/US reaction at 36 h. Based on the degradation products identified, a two-stage reduction/oxidation degradation mechanism was proposed. During the first stage, which was reductive debromination, the major reductive activity of nZVI was efficiently enhanced in the presence of nano Fe_3O_4 , which served as a catalyst to improve the stability of the nZVI nanoparticles and accelerate electron transfer, enhancing the degradation efficiency of BDE209. During the second stage, the oxidative ring-opening, the debromination products of BDE209 were proved to be attacked by abundant hydroxyl radicals generated both in the solution and on the surface of the $\text{Fe}^0@\text{Fe}_3\text{O}_4$ nanoparticles. Thus, this work provides an efficient method to achieve the complete ring-opening of PBDEs using iron-based nanomaterials.

© 2016 Elsevier B.V. All rights reserved.

1. Introduction

Polybrominated diphenyl ethers (PBDEs), which were extensively used as brominated flame retardants over the past decades in various industrial and consumer products [1], were proved to be toxic to the human nervous, endocrine and immune systems [2–4]. With the greatest use of decabromodiphenyl ether (BDE209) among the commercial PBDE products [5], developing efficient technologies to control the contamination of PBDEs (especially the BDE209) has generated deep concern [6]. BDE209, fully brominated diphenyl ether, is strongly resistant to oxidation due to the powerful electron-withdrawing ability of its bromine substituents [7,8]. Therefore, biodegradation [9,10], photodegradation [11,12]

and nanomaterials [5,13] are the three most widely studied reductive strategies for the degradation of BDE209.

Nano zero valent iron (nZVI) and its modified material are frequently used in the reductive debromination of PBDEs due to its large specific surface area, strong reduction ability and easy preparation. Zhuang et al. reported that BDE209 can be efficiently debrominated by nZVI to monobromodiphenyl ether [1]. Yu et al. found that BDE209 can be more efficiently degraded by nZVI when the nanoparticles(NPs) are preloaded on smectite [14]. However, although these reduction methods above successfully debrominate BDE209, they fail to further degrade the PBDEs into short-chain aliphatic compounds or CO_2 . Especially, some less or non-brominated products [15] still pose a threat to the environment, which can be more toxic with poorer biodegradability when compared with the aliphatic products [6,16,17]. Therefore, it is crucial to achieve a further degradation and ring-opening of BDE209.

To the best of our knowledge, however, only a few feasible strategies for the ring-opening degradation of BDE209 have been reported, and existing methods are primarily focused on the photo-

* Corresponding author at: School of Chemistry and Environment, South China Normal University, Guangzhou 51006, China.

E-mail address: zhqfang@scnu.edu.cn (Z. Fang).

tocatalytic oxidation of BDE209. An et al. found that BDE209 can be debrominated and then broken into short-chain carboxylic acids by photocatalysis using TiO_2 -immobilised montmorillonite [18]. Huang et al. also reported a TiO_2 -mediated photocatalytic strategy for the efficient debromination and ring-opening of BDE209 [19]. Both of the two studies take advantage of the strong oxidation capacity of hydroxyl radicals ($\cdot\text{OH}$). Moreover, it is also worth mentioning that nZVI and its modified materials exhibits high activity towards the low brominated diphenyl ethers and other halogenated organic compounds in Fenton-like oxidation systems [20–22]. Xu et al. reported that 4-chloro-3-methyl phenol can be removed completely in a heterogeneous Fenton-like system with nZVI as a catalyst [21]. In the study of Luo et al. (biphenyl ether) DPE can be degraded efficiently and mineralized in the $\text{Fe}/\text{Ag}/\text{H}_2\text{O}_2$ system subject to ultrasound (US) treatment [22]. Lin et al. also described a Fenton-like reaction system in which PCB28 was degraded with 99% efficiency within 48 h and mineralized using goethite [23]. The findings of these studies above confirm that $\cdot\text{OH}$ radicals are capable of attacking of low brominated BDEs and other water soluble halogenated organic compounds. Nevertheless, as BDE209 is fully brominated diphenyl ether, it is extremely chemically stable due to its symmetrical structure. Therefore, we wondered if we could build an efficient oxidation system to realize the further ring-opening degradation of BDE209 by the nZVI based material, which is also the main purpose of this paper.

Some researchers reported that nZVI particles are vulnerable to aggregation and surface passivation, which strongly decreases the electron transfer and reductive reactivity of nZVI [14,24,25]. Thus, in this study, we prepared the nano $\text{Fe}^0@\text{Fe}_3\text{O}_4$ composite that the nZVI particles attached to the surface of Fe_3O_4 tightly, overcoming the aggregation and passivation problems of nZVI. It not only accelerated the electron transfer to target pollutants so that it made the most use of the nZVI, but also improved the stability of nZVI particles. The composite was then used in the reductive/oxidative coupled reaction system assisted with US to degrade BDE209. The reaction system in our research combined the strong reduction ability of $\text{Fe}^0@\text{Fe}_3\text{O}_4$ nanocomposite with the oxidation activity of $\cdot\text{OH}$ radicals generated by a Fenton-like reaction, achieving the ring-opening of BDE209. The reduction and subsequent oxidative degradation of BDE209 were performed and analyzed. Based on the results of nanomaterial characterization, the kinetic study, product determination and reactive species identification, a detailed degradation pathway and mechanism was proposed. This reaction system offers a promising method of achieving the complete ring-opening degradation of PBDEs.

2. Experimental

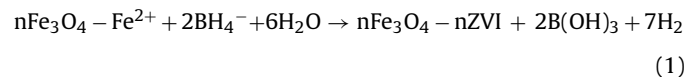
2.1. Materials and chemicals

A standard solution of BDE209 was purchased from Cambridge Isotope Laboratories (CIL, Andover, MA) and used to establish a calibration curve. BDE209 (>98%) was purchased from Aladdin (Shanghai, China) and used as the degradation sample. Ferrous sulphate ($\text{FeSO}_4 \cdot 7\text{H}_2\text{O}$, 99%), ferric chloride ($\text{FeCl}_3 \cdot 6\text{H}_2\text{O}$, >99%) and sodium borohydride (NaBH_4 , >98%) were purchased from Damao Chemical Reagent Factory (China). The high performance liquid chromatography (HPLC) grade methyl alcohol, tetrahydrofuran (THF) and acetonitrile were obtained from Aladdin (Shanghai, China).

2.2. Preparation and characterization of $\text{Fe}^0@\text{Fe}_3\text{O}_4$ nanoparticles

First, the Fe_3O_4 NPs were prepared by the co-precipitation method. This synthesis method was described in detail in reference

[26]. A brief description of the preparation method is illustrated in the supporting information Section S1. The prepared Fe_3O_4 NPs (1.28 g) were then mixed with the FeSO_4 solution (1.589 g $\text{FeSO}_4 \cdot 7\text{H}_2\text{O}$ was dissolved in 35 mL ethanol/water solution). Then the NaBH_4 solution (0.434 g) was added drop-wise to the mixed solution to reduce Fe^{2+} , forming the nZVI particles, and NaBH_4 was all reacted in equimolar ratio (Eq. (1)) [20].



The $\text{Fe}^0@\text{Fe}_3\text{O}_4$ nanoparticles (1.28 g Fe_3O_4 , 0.32 g nZVI) were collected by magnetic separation and washed by ultra-pure water to neutral pH. Finally, the $\text{Fe}^0@\text{Fe}_3\text{O}_4$ NPs were re-dispersed into 50 mL of ultra-pure water for further use.

The morphology and particle size of the resulting $\text{Fe}^0@\text{Fe}_3\text{O}_4$ NPs were analyzed using high resolution transmission electron microscopy (TEM) (HRTEM, TECNAI, G20, FEI, USA), field-emission TEM (Tecnai G2 F20, FEI, USA) and scanning electron microscopy (SEM, NoVaTM Nano SEM 250, FEI, USA). X-ray energy dispersive spectroscopy (EDS) was used to identify the element composition and distribution. Brunnaer-Emmett-Teller (BET) surface area analysis of the $\text{Fe}^0@\text{Fe}_3\text{O}_4$ NPs was performed by nitrogen adsorption-desorption using an ASAP2020 M surface analyzer (Micromeritics Instrument Corp., USA). X-ray diffraction (XRD) patterns were obtained using an X-ray diffractometer (DMAX 2200 VPC, Rigaku, Japan) emitting $\text{Cu K}\alpha$ radiation. The acceleration voltage and applied current were 40 kV and 30 mA, respectively. The magnetic properties of the composite material at 27 °C were measured using a vibrating-sample magnetometer (MPMS XL-7, Quantum Design, USA). The Zeta-potential of the nanomaterials was measured by the Malvern Zetasizer Nano ZS90 nanoparticle size and zeta potential instrument.

2.3. Degradation of BDE209

We noted that the proportion of water in the solvent has an important impact on the degradation of BDE209 [27]. Researchers have reported that the larger the proportion of water in the reaction system, the faster the degradation of BDE209 [19,27]. In addition, to prevent the organic solvent from quenching the hydroxyl radicals, our experiments were carried out in a system with 98% water content. The reaction solution (10 mg/L, 15 mL) was prepared by diluting the BDE209 stock solution (500 mg/L in pure THF) with Milli-Q water, and then the suspension was ultrasonically mixed for 1 min so that the BDE209 can be mixed in the reaction system uniformly [19]. Besides, all the Milli-Q water the experiment used was deoxygenated by purging with N_2 gas for 30 min before use. In the above systems, it should be pointed out that no BDE209 was detected to be adsorbed on the reactor. The prepared 150 mg $\text{Fe}^0@\text{Fe}_3\text{O}_4$ composite was added to a 40-mL vial containing 15 mL of the PBDE solution, and then covered with PTFE lids. The sacrificial experiments were carried out under US conditions and the US frequency was set at 25 kHz at a temperature of 35 ± 2 °C, and the initial pH was 7.1. Blank samples (without the addition of nanoparticles) were treated the same as described above. Each experiment was run in triplicate. At given time intervals, samples were taken out and a powerful magnet was then used to attract $\text{Fe}^0@\text{Fe}_3\text{O}_4$ particles at the bottom of bottles so that the aqueous solutions can be taken out. The supernatants and the compounds adsorbed on the $\text{Fe}^0@\text{Fe}_3\text{O}_4$ particles were then analyzed separately. The BDE209 in the supernatants was extracted by *n*-hexane (1:1, v/v) [28]. All the extractions were performed three times. The adsorbed BDE209 on the $\text{Fe}^0@\text{Fe}_3\text{O}_4$ particles was completely desorbed by

acetonitrile [29]. Our preliminary experiments and research [29] have confirmed that the BDE209 adsorbed on the nanoparticles can be extracted with a high efficiency and was not influenced by the extraction method.

2.4. Analysis of degradation products

The concentration of BDE209 was determined using an HPLC system (HP1100, Shimadzu, Japan) fitted with an SGE C18 column (250 mm × 4.6 mm) and coupled with an ultraviolet detector (SPD-10AV) set at $\lambda = 240$ nm. A 100% methanol solution at a flow rate of 1.0 mL/min was used as the mobile phase. The sample size was 20 μ L and quantification was done with a calibration curve of BDE209 standards.

During the degradation process, BDE209 not only existed in the supernatants but also adsorbed on the $\text{Fe}^0@\text{Fe}_3\text{O}_4$ nanoparticles. Besides, the purpose of our experiment system design is to achieve a ring-opening of BDE209 rather than simply adsorption of BDE209 by nanomaterials without degradation, so we defined the removal efficiency and degradation efficiency separately to evaluate the degradation process precisely.

$$\text{Removal efficiency (\%)} = \frac{m_0 - m_{\text{super}}}{m_0} \times 100\%$$

$$\text{Degradation efficiency (\%)} = \frac{m_0 - m_{\text{super}} - m_{\text{extra}}}{m_0} \times 100\%$$

where m_0 is the initial mass of BDE209 in the whole reaction system before the degradation process started; m_{super} is the mass of BDE209 in the supernatants and m_{extra} is the mass of BDE209 adsorbed by the $\text{Fe}^0@\text{Fe}_3\text{O}_4$ NPs.

The concentration of Br^- ions in reaction solution was monitored by ion chromatography (ICS-900) equipped with a conductivity detector and a 250/4.0 mm column (Dionex AS19).

The supernatants and the compounds adsorbed on the $\text{Fe}^0@\text{Fe}_3\text{O}_4$ particles were then analyzed separately. The debromination products of BDE209 were identified using GC-MS the analysis parameters and details can be seen in supporting information (Section S2). The polar degradation products dissolved in the reaction supernatant were identified by many techniques including GC-MS full scanning LC-MS/MS and FT-IR. A Fourier transform infrared (FTIR) spectrophotometer (IRPrestige-21, Shimadzu, Japan) was used to identify the structure of the degradation products preliminarily. GC-MS and LC-MS/MS were also adapted to identify the degradation intermediates. The analysis parameters can be seen in supporting information (Sections S3 and S4).

The electron paramagnetic resonance (EPR) technology was used to identify the activity radicals. In this study, 100 μ L samples were collected from the degradation reaction solution, and immediately mixed with 20 μ L 0.2 mol/L 5,5-dimethyl-1-pyrroline N-oxide (DMPO) to form DMPO-radicals adduct. The EPR spectra were obtained on a Bruker EPR 300E with a microwave bridge (receiver gain, 1×10^5 ; modulation amplitude, 2 Gauss; microwave power, 10 mW; modulation frequency, 100 kHz). The fluorescent spectroscopy technique with terephthalic acid (TA) was used to preliminarily quantify the amount of radicals in the suspension. Terephthalic acid readily reacts with and produces a highly fluorescent product, 2-hydroxyterephthalic acid [30–32]. The method is rapid, sensitive, and specific, needing only simple standard fluorescent spectroscopy instrumentation [33]. The Hitachi F-2700 type fluorescence spectrophotometer excited at 315 nm was used to record the fluorescence emission spectra of the fluorescent product when using the nanomaterial as the heterogeneous Fenton-like catalyst.

3. Results and discussion

3.1. Characterization of $\text{Fe}^0@\text{Fe}_3\text{O}_4$ NPs

The surface morphology of the $\text{Fe}^0@\text{Fe}_3\text{O}_4$ NPs was shown in Fig. 1(a). The fresh $\text{Fe}^0@\text{Fe}_3\text{O}_4$ NPs were generally distributed uniformly and connected in chains, due to magnetic dipole interactions and the nanometer-size effect. The close-up image shown in Fig. S1(c) revealed those nanoparticles were generally spherical in shape with the majority in the size range of 100–200 nm. The TEM analysis results of the $\text{Fe}^0@\text{Fe}_3\text{O}_4$ nanoparticles were provided in Fig. 1(b), showing that the core particles were surrounded by a layer of small spherical particles. We assumed that these small spherical particles were nZVI particles, and that the core of the composite was Fe_3O_4 NPs. The EDS results provided evidence for this assumption. The EDS study was performed to determine the element distribution of the core (Fig. 2(a)) and the outer layer (Fig. 2(b)) of the NPs. As shown in (Fig. S2), the presence of oxygen (O) in both the core and the outer layer was confirmed, providing further evidence that the inner part of the composite was made up of Fe_3O_4 . The detection of O in the outer layer can be attributed to the reactivity to oxidation of nZVI particles. We assumed that a layer of iron-oxide film was formed during either preparation or analysis due to the strong reduction ability of nZVI [34,35]. The presence of such an iron-oxide film was confirmed by TEM, as displayed in the inset of Fig. 1(b).

Based on the characterization results above, we drew a schematic diagram of the probable structure of the composite (Fig. 1(d)), depicting a core of Fe_3O_4 NPs surrounded by a layer of spherical nZVI NPs. The XRD patterns for the nano composite were shown in Fig. 3(a). The peaks at 2θ values of 35.5°, 43.1°, 53.5° and 62.6° were indexed as diffractions of (220), (400), (422), (511) and (440) respectively, (according to the JCPDS PDF#65-3107), proving the presence of Fe_3O_4 in the composite. However, only a small broad peak was observed in the typical nZVI diffraction region (at a 2θ value of 44.9°), suggesting that the nZVI constituent of the $\text{Fe}^0@\text{Fe}_3\text{O}_4$ NPs was in an amorphous state [36]. As shown in the HRTEM results, the lattice pattern that was observed in the particles with fringe-spacing values of 0.498 nm can be assigned to the (111) reflection of Fe_3O_4 [37]. According to the results of the XPS analysis (Fig. 3(b)), the spectrum of Fe 2p (inset in S1, Fig. S3(b)), with peaks at 710.6 eV and 724.4 eV of Fe 2p3/2 and 2p1/2 respectively demonstrated the existence of Fe_3O_4 nanoparticles (NPs) obviously [38–40]. However, the typical Fe⁰ peak at 706.9 eV was not obvious, which may be ascribed to the nZVI loading being 21 wt% in the composite and the reactivity to oxidation of nZVI particles. Besides, the XPS gives information more about the superficial part [36], and the presence of such an iron-oxide film was confirmed by TEM, as displayed in the inset of Fig. 1(b). Therefore, the XPS results further confirmed that nZVI particles were enclosed by a layer of iron-oxide film.

The specific surface area of the $\text{Fe}^0@\text{Fe}_3\text{O}_4$ composite was $37.33 \text{ m}^2 \text{ g}^{-1}$, which is higher than the reported Fe_3O_4 supported nanomaterials [20] and pure nZVI ($26 \text{ m}^2 \text{ g}^{-1}$). The BET surface area, pore size and pore volume of the nanocomposite are shown in Fig. S1 and Table S1, suggesting that the composite had a narrow pore-size distribution. The room temperature magnetization curves for the $\text{Fe}^0@\text{Fe}_3\text{O}_4$ NPs can be seen in Fig. S1 (b). The saturation magnetization (M_s) value of the composite (96.5 emu g^{-1}) was higher than that of pure nZVI (82.2 emu g^{-1}) and the Fe_3O_4 (77.4 emu g^{-1}) particles. The highest value of M_s guaranteed a nice magnetic-separation performance when an external magnetic field was applied, which is a significant advantage for nanoparticles to be recycled in an aqueous environment [41].

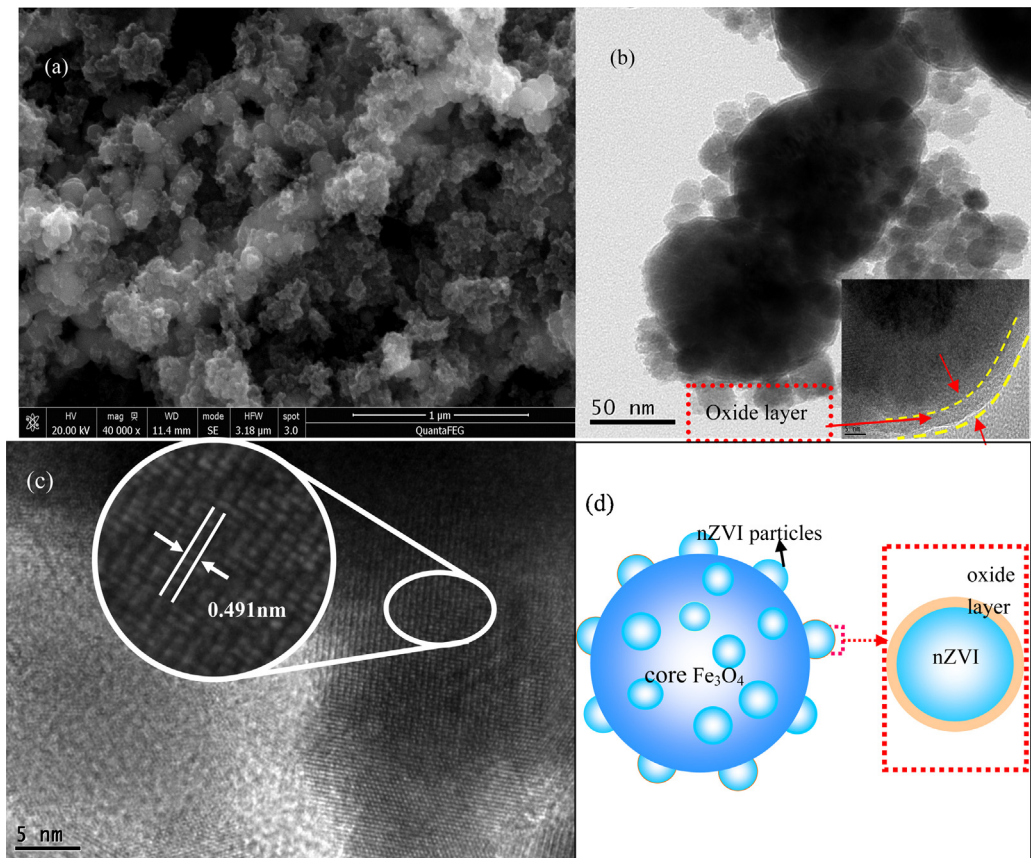


Fig. 1. (a) SEM images of $\text{Fe}^0@\text{Fe}_3\text{O}_4$ nanoparticles; (b) TEM images of $\text{Fe}^0@\text{Fe}_3\text{O}_4$ nanoparticles; (c) HRTEM images of the $\text{Fe}^0@\text{Fe}_3\text{O}_4$ nanoparticles; (d) the schematic diagram of the $\text{Fe}^0@\text{Fe}_3\text{O}_4$ nanoparticles' structure.

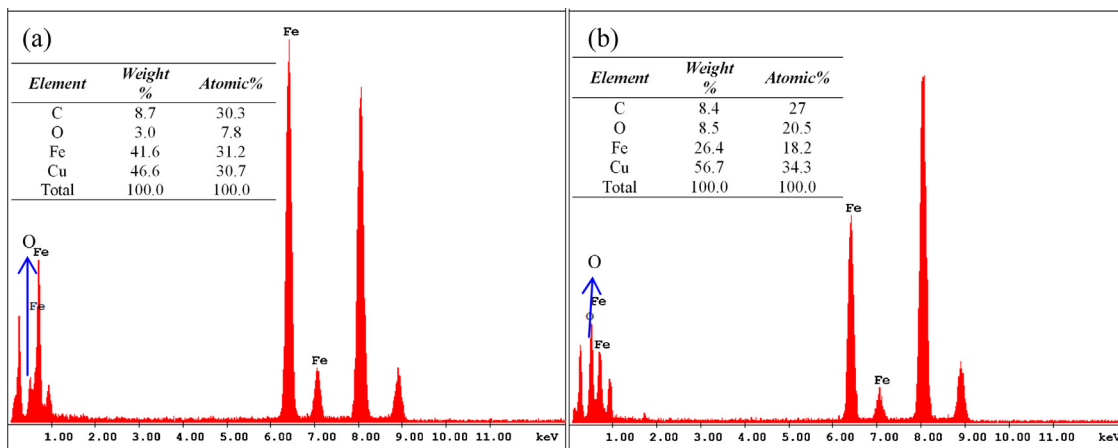


Fig. 2. EDS spectra of the core (a) and the outer layer (b) of $\text{Fe}^0@\text{Fe}_3\text{O}_4$ nanoparticles.

3.2. The catalytic activity of the $\text{Fe}^0@\text{Fe}_3\text{O}_4$ composite material

We defined the following three major factors influencing BDE209 degradation: US treatment, the addition of H_2O_2 and the addition of $\text{Fe}^0@\text{Fe}_3\text{O}_4$ NPs (given as US, H_2O_2 and NP). The degradation experiments of BDE209 were conducted in US, H_2O_2 , NP, US/ H_2O_2 , NP/US, NP/ H_2O_2 and NP/US/ H_2O_2 systems for 48 h each and the time point of the H_2O_2 addition was set at 36 h in the groups which need the addition of H_2O_2 (H_2O_2 , US/ H_2O_2 , NP/ H_2O_2 and NP/US/ H_2O_2).

As shown in Fig. 4(a), only a slight removal and degradation efficiency (less than 5%) of BDE209 was attained in the control groups

subject to H_2O_2 or US alone. This indicates that BDE209 cannot be degraded either by the US cavitation effect or by strong oxidizers, due to its structural stability. Luo et al. [22] reported similar findings for the degradation of BDE47 using a Fenton-like method with Fe/Ag NPs. However, when the $\text{Fe}^0@\text{Fe}_3\text{O}_4$ NPs were introduced to the degradation system, the BDE209 removal efficiency was notably enhanced, reaching 100% at 48 h in all the NP, NP/US and NP/US/ H_2O_2 groups.

Moreover, comparison of the degradation performance of the $\text{Fe}^0@\text{Fe}_3\text{O}_4$ NPs under the eight sets of conditions revealed that US treatment and H_2O_2 had great influence on degradation efficiency. Specifically, the highest degradation efficiencies (75% and above)

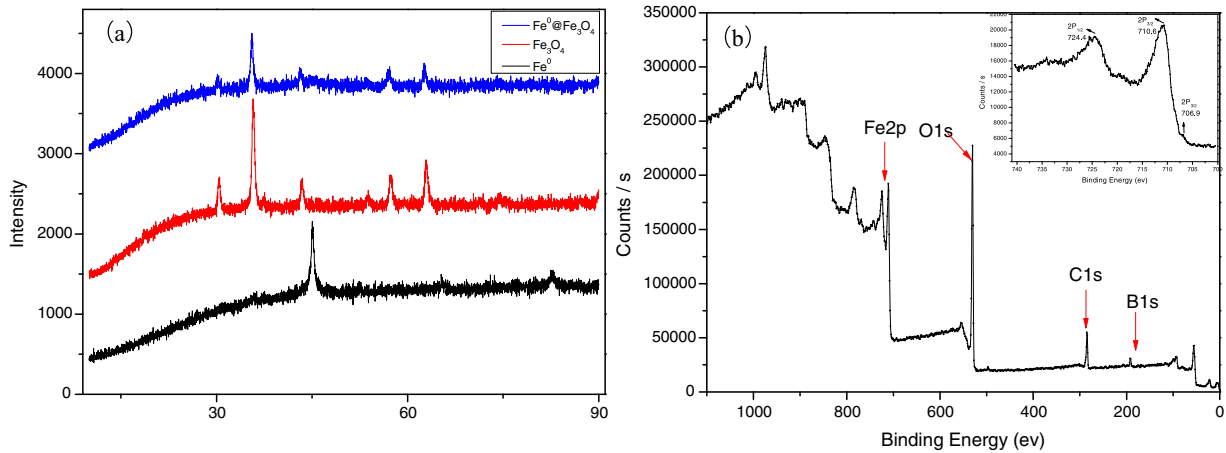


Fig. 3. (a) XRD and (b) XPS patterns for $\text{Fe}^0@\text{Fe}_3\text{O}_4$ nanoparticles.

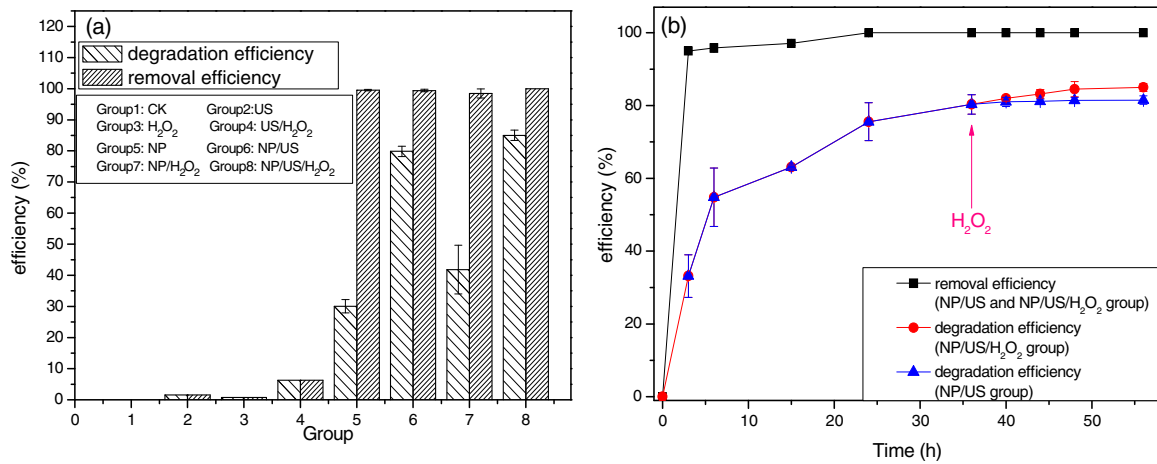


Fig. 4. (a) Degradation and removal of BDE209 under different conditions; reaction time: 48 h; (b) Removal efficiency and degradation efficiency in the NP/US and NP/US/ H_2O_2 system (US conditions: 25 kHz, 100 W, 35 °C; initial concentration of BDE209 = 10 mg/L; pH = 7.1; $[\text{Fe}^0@\text{Fe}_3\text{O}_4$ composite] = 0.010 g/ml).

were observed in Group 6 (NP/US: 79%) and Group 8 (NP/US/ H_2O_2 : 85%) as illustrated in Fig. 4(a). This finding suggested that there was a synergistic effect among NP, US and H_2O_2 , which was also reported by Huang et al. [26] and Luo et al. [22].

The variation in removal efficiency and degradation efficiency over time of Group 6 and Group 8 was shown in Fig. 4(b). The removal efficiency reached up to 90% in only 3 h, which can be attributed to the large specific area of the $\text{Fe}^0@\text{Fe}_3\text{O}_4$ NPs. In contrast, degradation efficiency reached only 30% during the initial reaction stage (the first 3 h of the whole reaction process), indicating that the surface adsorption played a vital role in the initial reaction stage. In addition, as shown in Fig. 4(b), the degradation efficiency in the NP/US group increased consistently before reaching equilibrium at 80% in 36 h. This is much higher than that reported for many other nanoscale iron-based materials [5,29], indicating the advantages of the $\text{Fe}^0@\text{Fe}_3\text{O}_4$ composite in BDE209 degradation. After that, the degradation efficiency increased only slightly in the subsequent 12 h, reaching 81% at 48 h, which revealed that equilibrium was reached in the time point of 36 h.

However, it is interestingly noted that as shown in Fig. 4(b), the degradation efficiency increased by 4 percentage points as time prolonged from 36 h to 48 h after the addition of H_2O_2 at 36 h (i.e. under NP/US/ H_2O_2 condition). However, the degradation efficiency had no increase as time prolonged from 36 h to 48 h in the NP/US system without the addition of H_2O_2 . Therefore, we tentatively deduced that the BDE209 had been further oxidatively

degraded by the addition of H_2O_2 after reductive debromination by the $\text{Fe}^0@\text{Fe}_3\text{O}_4$ NPs. To confirm this deduction, we investigated the degradation products using FTIR, GC-MS and LC-MS/MS.

3.3. Analysis of degradation intermediates

3.3.1. Debromination intermediates

To identify the intermediate products, an extraction was carried out after the magnetic separation of the $\text{Fe}^0@\text{Fe}_3\text{O}_4$ NPs as the hydrophobic debromination products of BDE209 were deemed to have been adsorbed onto the composite surface [19,28]. The identification methods are described in detail in Section S2. According to the GC-MS chromatograms of BDE209 degradation under the NP/US (SI Fig. S2(a)) and NP/US/ H_2O_2 (SI Fig. S2(b)) conditions, the $\text{Fe}^0@\text{Fe}_3\text{O}_4$ NPs were able to rapidly debrominate BDE209 to a wide range of PBDEs, from di- to nona-BDEs under the NP/US/ H_2O_2 condition. In the absence of H_2O_2 , however, the parent BDE209 degraded only to tetra- and nona-BDEs, indicating that further debromination of the PBDEs occurred after the introduction of H_2O_2 .

Due to the lack of certain commercial PBDE standards at the time of the experiment, 26 kinds of typical PBDEs were quantified in our experiments [42]. Based on the quantitative results, the distribution of homologues under the NP/US and NP/US/ H_2O_2 conditions was shown in Fig. 5(a). The amount of penta-BDEs to di-BDEs in the NP/US/ H_2O_2 condition was higher than that of the

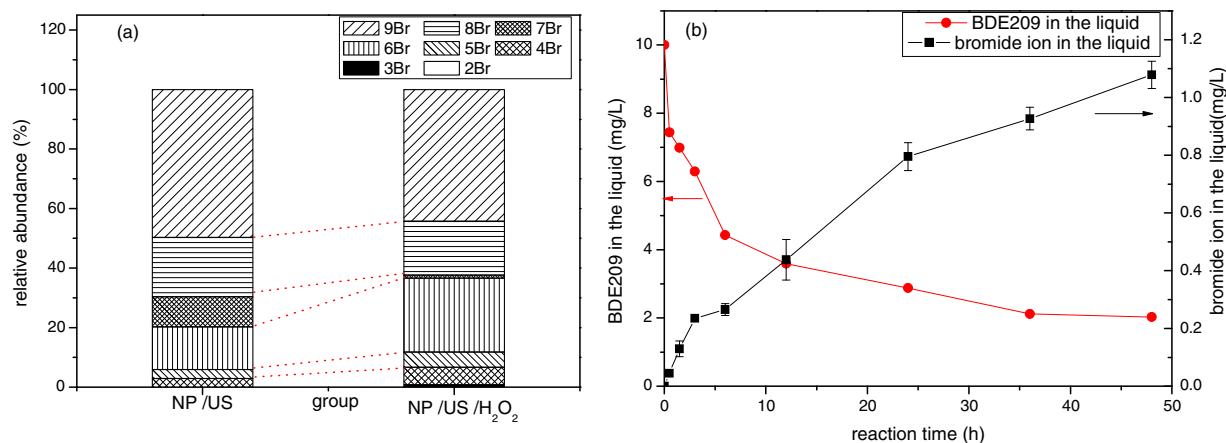


Fig. 5. (a) Percentage distribution of di-BDEs to deca-BDEs produced from BDE209 under NP/US conditions and NP/US/H₂O₂ conditions; (b) the variation of bromide-ion concentration under NP/US/H₂O₂ conditions: 25 kHz, 100 W, 35 °C; initial concentration of BDE209 = 10 mg/L; pH = 7.1; [Fe⁰@Fe₃O₄ composite] = 0.010 g/ml.

NP/US group, while the amount of high brominated diphenyl ethers (penta- to deca-BDEs) in the NP/US/H₂O₂ condition was lower than the NP/US condition. These results confirmed our assumption that the addition of H₂O₂ promoted the further debromination of high brominated diphenyl ethers, leading to a decrease of high brominated diphenyl ethers and the accumulation of low brominated diphenyl ethers. We also measured the concentration of bromide ion in the reaction system. The concentration variation of bromide ions was shown in Fig. 5(b). Notably, the amount of bromide ions released into the system continued increasing substantially after 36 h, though the concentration of BDE209 had nearly reached equilibrium at that time. This finding evidenced that the catalytic activity of the Fe⁰@Fe₃O₄ NPs was not inhibited by the addition of H₂O₂; on the contrary, further debromination and degradation of PBDEs occurred in the reaction system, revealing that the addition of H₂O₂ can promote the debromination of BDE209 and the PBDE intermediates by the Fe⁰@Fe₃O₄ nanocomposite.

3.3.2. Identification of ring-opening products

In order to verify that the ring-opening of BDE209 was caused by the addition of H₂O₂, various detection methods, such as FTIR, GC-MS and LC-MS/MS, were adopted. First, the variations in the supernatants of the NP/US/H₂O₂ and NP/US degradation system were checked using FTIR. As shown in Fig. 6, an absorption band was observed within a wavenumber of 1716 cm⁻¹, which was mainly caused by the stretching vibration of the C=O. Meanwhile, the absorption peaks observed at 1600 cm⁻¹ and 1395 cm⁻¹ were caused by the asymmetrical stretching vibration and the symmetrical stretching vibration of O=C—O— [19], respectively. These typical features signaled the formation of certain carboxylic derivatives, which were supposed to be generated from ring-opening products. In contrast, these adsorption bands did not appear in the reaction supernatants in the NP/US group. Based on the FTIR results, we concluded preliminarily that the addition of H₂O₂ caused the ring-opening of BDE209.

In addition, GC-MS full scanning was performed to identify the ring-opening products specifically. Prior to GC-MS scanning, trimethylsilylation was carried out using bis(trimethylsilyl)trifluoroacetamide (BSTFA) [22,43]. The identification methods were described in detail in supporting information Section S3. Seven ring-opening products were detected (Table 1) and the corresponding GC-MS spectra were shown in Fig. S4(a). Information on the chemical structure and retention time of the intermediates was provided in Table 1, and the mass spectra of these ring-opening products identified with BSTFA derivatization can be observed in Fig. S6. Using a standard spectral

library, the seven ring-opening by-products were identified as the following: glycolic acid; 4-hydroxy butyric acid; 1,6-hexanediol; 1,3-propanediol ether; 3,4-dihydroxy-n-butyric acid; 1,2,4-trihydroxybutane; 2-hydroxy butanedioic acid; 2-hydroxy,4-methyl valeric acid. However, we did not find these compounds in the reaction supernatants of the NP/US group as shown in Fig. S4(b), which testified to the vital role the H₂O₂ played in the degradation system.

Besides, in order to remove the possible products arising from the THF degradation, we designed control experiments. The 15 mL BDE209-free reaction solution containing only 2%THF and 98% water was treated by the same procedures. The resulting degradation solution was also monitored by GC-MS after the derivatization, and the obtained spectra were shown in Fig. S5 (Supporting information). However, we did not find any ring-opening products that Table 1 listed. Thus the seven ring-opening by-products identified were oxidative ring opening products of BDEs.

The components extracted from the reaction supernatants were further analyzed by LC-MS/MS, as shown in Fig. S8. Some of the compounds were deduced by analyzing the fragment peaks in the second-order mass spectrum. The mass fragment ions (SI Fig. S8(a)) at the *m/z* values of 255/257/259 ([M-2H]⁻), 237/235 ([M-OH]⁻), and 45 ([COO]⁻), 79, 81 ([Br]⁻) were assigned to C₅H₄Br₂O₂ (M_r: 255.9). Meanwhile, the mass fragment ions (SI Fig. S8 (b)) at *m/z* values of 378/380/382 ([M-2H]⁻), 362/364 ([M-OH]⁻), 333/335 ([M-COO]⁻) and 45 ([COO]⁻), 79, 81 ([Br]⁻) were assigned to C₆H₅Br₃O₄ (M_r: 380.83). The mass fragment ions (SI Fig. S8(c)) at the *m/z* values of 281/283/285 ([M-2H]⁻), 263/265 ([M-OH]⁻) and 45 ([COO]⁻), 79, 81 [Br]⁻ may be assigned C₆H₄Br₂O₃ (M_r: 283.9). Detailed information about the three organic compounds can be seen in Supporting information Section S4.

3.4. Degradation pathway and possible mechanism

All of the results above confirmed that enhanced reductive debromination and subsequent oxidative ring-opening of BDE209 can be achieved in the reduction-oxidation coupling system we established. Based on the identified debromination products and ring-opening products (Fig. S2; Table 1; Fig. S7), a degradation pathway was proposed as shown in Fig. 7. The proposed degradation process included two stages: reductive debromination during the first 36 h, followed by oxidative ring opening (lasting for 12 h after the addition of H₂O₂).

To test our presumption of the whole degradation process, we compared the effects of other H₂O₂ dosing points on the degradation of BDE209, as shown in Fig. 6(b). When H₂O₂ was added at the

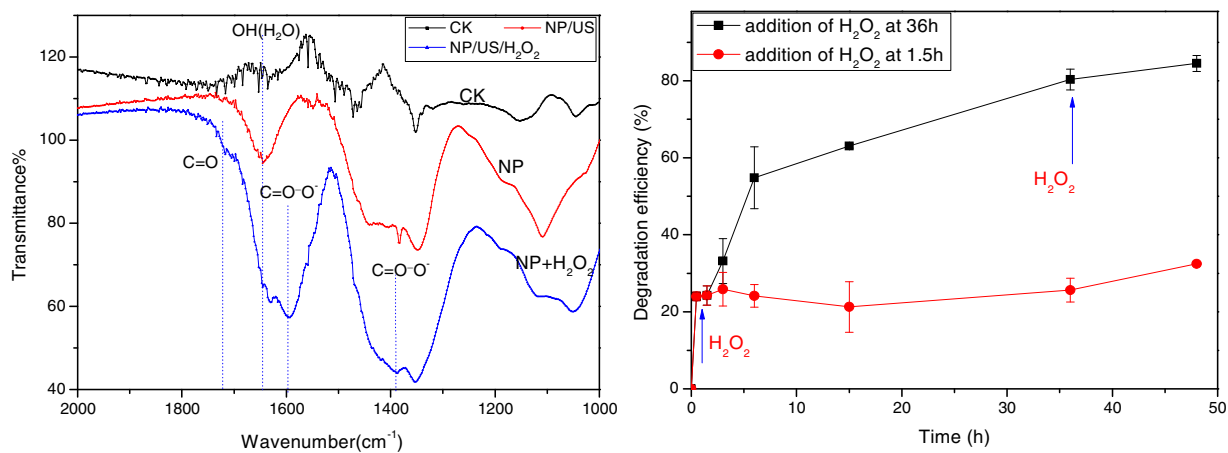


Fig. 6. (a) FTIR spectra of reaction supernatants under the NP/US and NP/US/H₂O₂ conditions; (b) effect of the H₂O₂ dosage point on the degradation of BDE209 (US conditions: 25 kHz, 100 W, 35 °C; initial concentration of BDE209 = 10 mg/L; pH = 7.1; [Fe⁰@Fe₃O₄ composite] = 0.010 g/ml).

Table 1
Identification of the intermediates of ring-opening products of BDE209 by GC/MS.

Proposed products	RT (min)	m/z	Name	Molecular structure
A	3.28 min	76	glycolic acid (C ₂ H ₄ O ₃)	
B	5.34 min	104	4-hydroxy butyric acid (C ₄ H ₈ O ₃)	
C	6.65 min	118	1,6-hexanediol (C ₆ H ₁₄ O ₂)	
D	7.30 min	134	1,3-propanediol ether (C ₆ H ₁₄ O ₃)	
E	7.71 min	120	3,4-dihydroxy-n-butryic acid (C ₄ H ₈ O ₄)	
F	9.06 min	106	1,2,4-trihydroxybutane (C ₄ H ₁₀ O ₃)	
G	9.49 min	134	2-hydroxy butanedioic acid (C ₄ H ₆ O ₅)	
H	9.65 min	132	2-hydroxy-4-methyl valeric acid (C ₆ H ₁₂ O ₃)	

time point of 1.5 h, the efficiency of BDE209 degradation was only about 25%, regardless of the presence of Fe⁰@Fe₃O₄ in the system, indicating that the early dosage of H₂O₂ inhibited the degradation of BDE209. The dosage of H₂O₂ at such an early stage (at the time point of 1.5 h) of the degradation reaction was assumed to have caused the surface passivation and oxidation of the Fe⁰@Fe₃O₄ nanomaterial, hindering mass transfer to and chemical reactions at reactive sites. The active reduction substances in the reaction system, i.e., Fe⁰ and Fe²⁺, were oxidized at the same time, resulting in a loss of reduction ability that seriously impeded the reductive debromination of BDE209. In contrast, when the H₂O₂ dose was administered at 36 h, the process of reductive debromination had almost reached equilibrium at that time. Notably, the degra-

tion efficiency continued rising instead of being suppressed after the dose of H₂O₂, ultimately reaching 85%, which supported our assumption that the first stage of the degradation process was a reductive debromination process.

In addition, during the second stage of the degradation process, i.e., after the dosage of the oxidant H₂O₂ at 36 h, the hydroxyl radicals formed by the addition of H₂O₂ attacked the lower brominated diphenyl ethers in the solution, leading to the formation of some hydroxylation intermediates. Meanwhile, some researchers have reported that those aromatic-[·]OH adducts were vulnerable to being attacked by [·]OH radicals and then oxidized to some short-chain carboxylic acids [44–46]. Thus the ring-opening of BDE209 to form short-chain carboxylic acids can be achieved in our system.

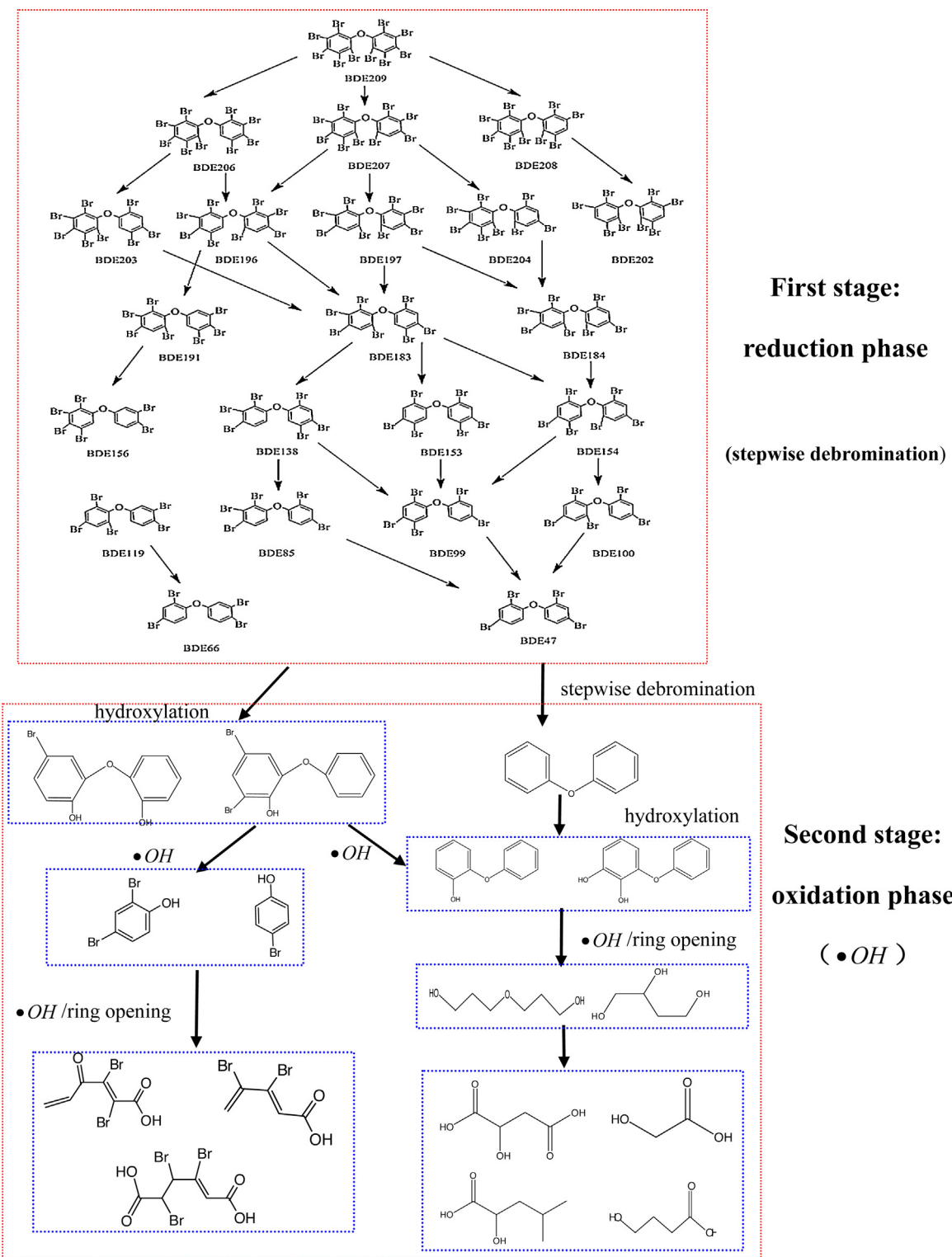


Fig. 7. Possible pathways for coupled reduction-oxidation degradation of BDE209 by $\text{Fe}^0@\text{Fe}_3\text{O}_4$ under NP/US/ H_2O_2 conditions.

3.4.1. Possible mechanism in the reduction phase: the role of nZVI and Fe_3O_4

The degradation and removal of BDE209 under NP/US/ H_2O_2 conditions were shown in Fig. 4(b). In the initial stages of reaction (at 3 h), the removal efficiency of BDE209 was 90%, but the degradation efficiency was only 33%, indicating that BDE209 was first adsorbed onto the surface of the $\text{Fe}^0@\text{Fe}_3\text{O}_4$ NPs, followed by gradual reductive debromination to lower brominated PBDEs, and

the stepwise debromination pathway [1,47] was shown in Fig. S3. As the nZVI particles were situated in the outer layer, the reductive debromination of BDE209 took place actively and easily in the former 36 h of the reaction.

To determine the roles of nZVI and Fe_3O_4 in the reductive debromination of BDE209 during the first stage, control experiments were conducted to compare the degradation efficiency of BDE209 by three different nano materials (nZVI, Fe_3O_4 , $\text{Fe}^0@\text{Fe}_3\text{O}_4$)

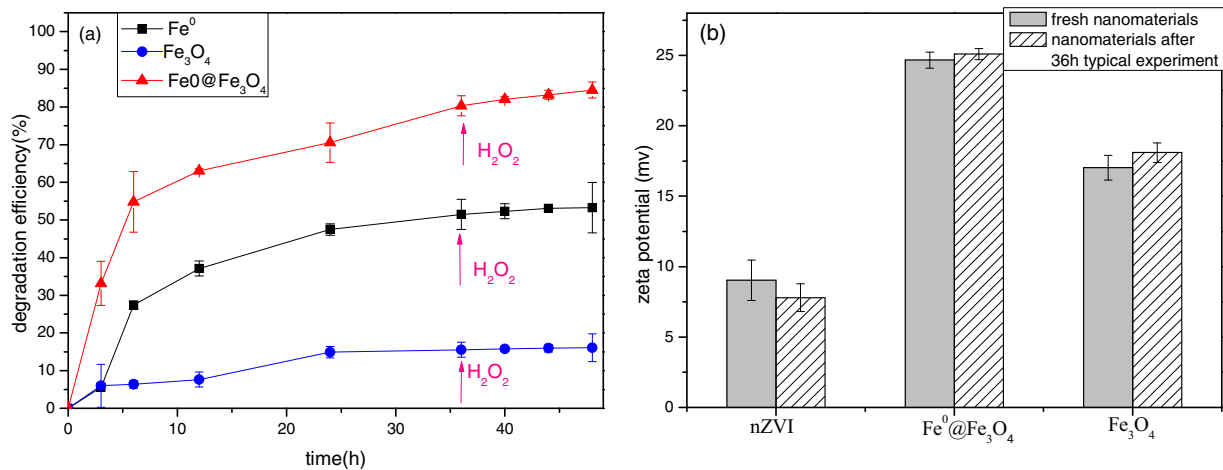


Fig. 8. (a) Degradation of BDE209 by three nanomaterials (nZVI, nano Fe_3O_4 and nano $\text{Fe}^0@\text{Fe}_3\text{O}_4$); (b) Zeta potential of the three nanomaterials (US conditions: 25 kHz, 100 W, 35 °C; initial concentration of BDE209 = 10 mg/L; pH = 7.1; [$\text{Fe}^0@\text{Fe}_3\text{O}_4$ composite] = 0.010 g/ml).

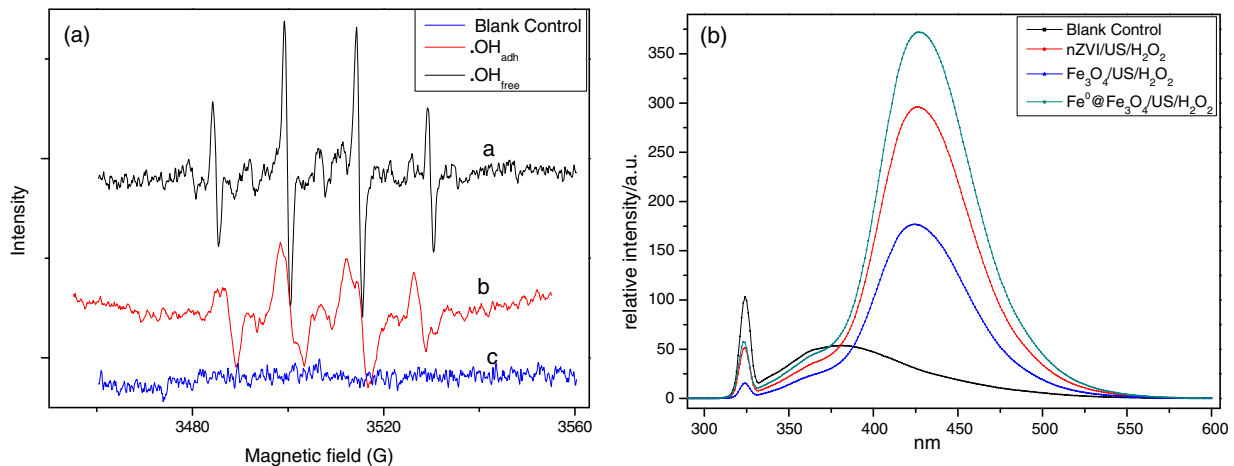


Fig. 9. (a) DMPO spin-trapping EPR spectra of hydroxyl radical in the: a) aqueous solution of the NP/US/ H_2O_2 degradation system, b) $\text{Fe}^0@\text{Fe}_3\text{O}_4$ NPs surface of the NP/US/ H_2O_2 degradation system c) blank control without the addition of H_2O_2 and $\text{Fe}^0@\text{Fe}_3\text{O}_4$ NP; (b) The relative intensities of hydroxyl radicals generated from three kinds of nanomaterial (nZVI, nano Fe_3O_4 , nano $\text{Fe}^0@\text{Fe}_3\text{O}_4$).

as shown in Fig. 8(a), each containing the same amount of nanomaterial dosage (10 g/L) and accompanied by US treatment. A degradation efficiency of only 15% was attained by the pure Fe_3O_4 NPs within 36 h before the addition of H_2O_2 , while a degradation efficiency of 52% was achieved by nZVI. The degradation of BDE209 using the $\text{Fe}^0@\text{Fe}_3\text{O}_4$ composite was significantly more efficient (80%) than that using either pure Fe_3O_4 or nZVI, implying that the nZVI particles played a major role in the reductive debromination process. It is also worth noting that the Fe^0 content of the $\text{Fe}^0@\text{Fe}_3\text{O}_4$ NPs was only 21%, suggesting that there might be a synergy effect of the constituents in the composite, thereby enhancing the relative rates of mass transfer to reactive sites and chemical reaction at reactive sites. Furthermore, as frequently reported in the studies about nZVI NPs [14,24,25], pure nZVI had a lower degradation efficiency than that of composite nanomaterials, because the aggregation problem and surface passivation of nZVI strongly limited electron transfer to target pollutants. However the composite when Fe_3O_4 supported the nZVI particles can overcome these problems. Magnetite (Fe_3O_4) has the property of magnetism, so nZVI particles can attach to its surface, preventing the aggregation of nZVI particles. Moreover, Fe^{2+} formed during the transfer between Fe^0 and Fe^{3+} in $\text{Fe}^0@\text{Fe}_3\text{O}_4$ also has reducing capacity, offering an alternative pathway for electron transfer from Fe^0 to BDE209. Therefore the introduction of

Fe_3O_4 enhanced the reductive debromination of BDE209. Besides, we noted that in the $\text{Fe}^0@\text{Fe}_3\text{O}_4$ reaction system the degradation of BDE209 was not inhibited after the addition of H_2O_2 . While in the nZVI system, the degradation efficiency changed little, which can be attributed to the passivation of nZVI surface after the addition of H_2O_2 . This result also illustrated the superiority of the $\text{Fe}^0@\text{Fe}_3\text{O}_4$ composite.

In addition, previous researchers have suggested that the stability of a reaction system was reflected in its zeta potential; the higher the zeta potential, the more stable the reaction system [48]. As shown in Fig. 8(b), we measured the zeta potential of the three kinds of materials (pH = 7.1) before and after the whole reaction process. Results showed that the composite has the highest zeta potential before and after the degradation experiment. It suggested that the introduction of Fe_3O_4 improved material stability of the $\text{Fe}^0@\text{Fe}_3\text{O}_4$ composite, enabling BDE209 to be tightly adsorbed on the surface of the composite and then reduced by the nZVI particles on the Fe_3O_4 surface, enhancing the efficiency of the reduction process. A similar finding was reported by Wu et al. [24].

In sum, nZVI played a reduction role in the reductive-debromination process, while Fe_3O_4 worked as a catalyst and a good support to overcome the aggregation and passivation problem of nZVI. It not only accelerated the electron transfer to target pol-

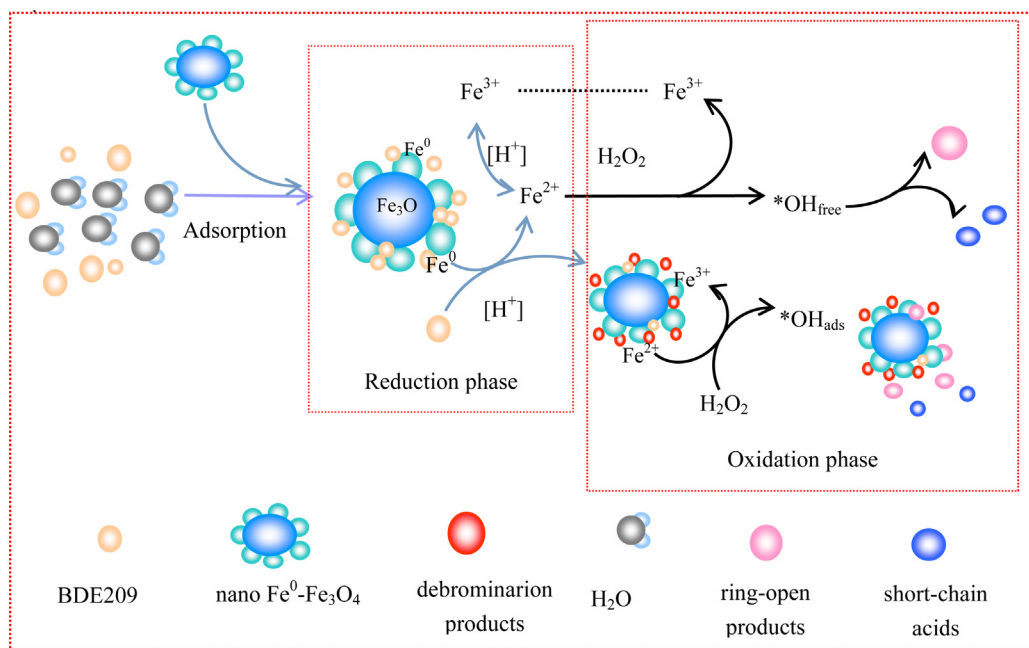


Fig. 10. Schematic diagram of the reaction mechanism of the degradation of BDE209 by $\text{Fe}^0@\text{Fe}_3\text{O}_4$.

lutants so that it made the most use of the nZVI, but also improved the stability of nZVI particles.

3.4.2. Possible oxidation mechanism in the second stage

Fenton's reagent process was induced by the production of Fe^{2+} during the first phase, leading to the generation of hydroxyl radicals in the second phase (oxidative ring-opening stage). Simultaneously, the debrominated products generated in the first stage were further attacked by $\cdot\text{OH}$ and then degraded to ring-opening products.

To determine the actual reactive species mediating these processes, a comparison test was conducted by testing the radical-scavenging effects of excess *n*-butanol [49] on the ring-opening products generated. GC-MS full scanning was employed to detect short-chain carboxylic acids or other ring-opening products if present. As shown in Fig. S6, short-chain carboxylic acids were not found in the GC-MS full scanning results, tentatively confirming the dominant role of $\cdot\text{OH}$ in the oxidation stage.

Moreover, many researchers have reported the combined effect of surface-bound $\cdot\text{OH}_{\text{ads}}$ on the surface of nanoparticles and $\cdot\text{OH}_{\text{free}}$ distributed in a solution [41,49,50], both of which attacked hydrophobic organic compounds to accomplish a ring-opening degradation or mineralization in a heterogeneous Fenton-like system. Due to the hydrophobicity of PBDEs, the debromination products were deduced to be further hydroxylated and ring-opened on the surface of the $\text{Fe}^0@\text{Fe}_3\text{O}_4$ NPs, consistent with the results reported by Luo et al. [22] and Zhang et al. [51]. In order to confirm this deduction, electron paramagnetic resonance (EPR) technique accompanied by the addition of the spin-trapping agent DMPO was performed. The detailed analysis parameters and procedures were shown in supporting information (Section S5). The EPR spectrum in the presence of $\text{Fe}^0@\text{Fe}_3\text{O}_4$ NPs, H_2O_2 and US displayed a 4-fold characteristic peak of the typical DMPO- $\cdot\text{OH}$ adduct with an intensity ratio of 1:2:2:1 [52–54], validating the existence of $\cdot\text{OH}_{\text{ads}}$ bound to the surface of the $\text{Fe}^0@\text{Fe}_3\text{O}_4$ NPs. The results also provide an auxiliary explanation of the increase in bromine ions after the addition of H_2O_2 , testifying to the oxidative debromination of the PBDEs by $\cdot\text{OH}_{\text{ads}}$. This finding is analogous to the oxidative degradation of BDE209 reported by Wang et al. [19] and An et al. [18]. Free

hydroxyl radicals ($\cdot\text{OH}_{\text{free}}$) were also clearly detected by EPR in the aqueous solutions, as shown in Fig. 9(a). Some hydrophilic organics or complete debromination products such as DPEs may be attacked by $\cdot\text{OH}_{\text{free}}$. However, we failed to detect the DPE products, perhaps due to the continual generation of $\cdot\text{OH}$ and the strong oxidizing capacity of $\cdot\text{OH}_{\text{free}}$. To confirm this assumption, we compared the amounts of $\cdot\text{OH}$ produced by the three kinds of material (nZVI, Fe_3O_4 and $\text{Fe}^0@\text{Fe}_3\text{O}_4$ composite) under the same reaction system as shown in Fig. 9(b). It is worth noting that the $\text{Fe}^0@\text{Fe}_3\text{O}_4$ composite yielded the largest amount of $\cdot\text{OH}$, unfolding its superiority as a heterogeneous reaction catalyst to the pure Fe_3O_4 and nZVI particles. This result also revealed that the Fe_3O_4 not only provided a good support for the ZVI particles but also worked as an excellent catalyst to improve the oxidation efficiency in the Fenton-like system.

Both the $\cdot\text{OH}_{\text{ads}}$ generated on the composite surface and the $\cdot\text{OH}_{\text{free}}$ produced by the continuous Fenton-like reaction between Fe^{2+} , Fe^{3+} and H_2O_2 attacked the intermediates generated in the first stage, achieving the further ring-opening degradation of BDE209. A schematic diagram of the probable reaction mechanisms underlying the reduction/subsequent oxidative ring-opening degradation of BDE209 by $\text{Fe}^0@\text{Fe}_3\text{O}_4$ in the NP/US/ H_2O_2 group is provided in Fig. 10.

4. Conclusion

Integrated catalyst of nZVI supported on magnetic Fe_3O_4 nanoparticles was chemically prepared and used in degradation of BDE209, reaching a 100% removal efficiency and 85% degradation efficiency. The ring-opening products of BDE209 were successfully identified in this paper, suggesting that BDE209 can be efficiently ring-opened by the $\text{Fe}^0@\text{Fe}_3\text{O}_4$ composite in the reduction-oxidation coupling system we established. We proposed a two-stage reduction/oxidation degradation mechanism. During the stage of reductive debromination, the reductive activity of nZVI was efficiently supported by Fe_3O_4 which worked as an excellent catalyst and accelerated electron transfer in the composite. In the oxidative ring-opening stage, both the $\cdot\text{OH}_{\text{ads}}$ generated on the composite surface and the $\cdot\text{OH}_{\text{free}}$ attacked the debrominated prod-

ucts of BDE209. This paper offers a promising method and catalyst to achieve a complete ring-opening of BDE209.

Acknowledgements

The authors acknowledge financial support from the National Natural Science Foundation of China (Grant No: 41471259) and Joint Foundation of NSFC-Guangdong Province (Grant No: U1401235). This work was also supported by the Guangdong Technology Research Centre for Ecological Management and Remediation of Water System.

Appendix A. Supplementary data

Supplementary data associated with this article can be found, in the online version, at <http://dx.doi.org/10.1016/j.apcatb.2016.07.005>.

References

- [1] Y. Zhuang, S. Ahn, R.G. Luthy, *Environ. Sci. Technol.* 44 (21) (2010) 8236–8242.
- [2] J. Chevrier, K.G. Harley, A. Bradman, M. Gharbi, A. Sjodin, B. Eskenazi, *Environ. Health Perspect.* 118 (10) (2010) 1444–1449.
- [3] L.H. Tseng, M.H. Li, S.S. Tsai, C.W. Lee, M.H. Pan, W.J. Yao, P.C. Hsu, *Chemosphere* 70 (4) (2008) 640–647.
- [4] T.A. McDonald, *Chemosphere* 46 (2002) 745–755.
- [5] Y.S. Keum, Q.X. Li, *Environ. Sci. Technol.* 39 (2005) 2280–2286.
- [6] S.J. Chen, A.H. Feng, M.J. He, M.Y. Chen, X.J. Luo, B.X. Mai, *Sci. Total Environ.* 444 (2013) 205–211.
- [7] C.Y. Sun, D. Zhao, C.C. Chen, W.H. Ma, J.C. Zhao, *Environ. Sci. Technol.* 43 (1) (2009) 157–162.
- [8] P.M. Bastos, J. Eriksson, J. Vidarson, Å. Bergman, *Environ. Sci. Pollut. Res.* 15 (2008) 606–613.
- [9] H.M. Stapleton, B. Brazil, R.D. Holbrook, C.L. Mitchelmore, R. Benedict, A. Konstantinov, D. Potter, *Environ. Sci. Technol.* 40 (15) (2006) 4653–4658.
- [10] J. He, K.R. Robrock, L. Alvarez-Cohen, *Environ. Sci. Technol.* 40 (14) (2006) 4429–4434.
- [11] C.H.Y. Sun, W. Chang, W.H. Ma, C.C. Chen, J.C. Zhao, *Environ. Sci. Technol.* 47 (2013) 2370–2377.
- [12] M. Lei, N. Wang, L.H. Zhu, Q.L. Zhou, G. Nie, H.Q. Tang, *Appl. Catal. B Environ.* 182 (2016) 414–423.
- [13] A. Li, C. Tai, Z.S. Zhao, Y.W. Wang, Q.H. Zhang, G.B. Jiang, J.T. Hu, *Environ. Sci. Technol.* 41 (2007) 6841–6846.
- [14] K. Yu, C. Gu, S.A. Boyd, C. Liu, C. Sun, B.J. Tepper, H. Li, *Environ. Sci. Technol.* 46 (2012) 8969–8975.
- [15] E.J. Kim, J.H. Kim, V. Bokare, Y.S. Chang, *Sci. Total Environ.* (2014), 470–471, 1553–1557.
- [16] J. Eriksson, N. Green, G. Marsh, A. Bergman, *Environ. Sci. Technol.* 38 (11) (2004) 3119–3125.
- [17] J.Z. He, K.R. Robrock, L. Alvarez-Cohen, *Environ. Sci. Technol.* 40 (14) (2006) 4429–4434.
- [18] T.C. An, J.X. Chen, G.Y. Li, X.J. Ding, G.Y. Sheng, J.M. Fu, B.X. Mai, K.E. O'shea, *Catal. Today* 139 (1–2) (2008) 69–76.
- [19] A.Z. Huang, N. Wang, M. Lei, L.H. Zhu, Y.Y. Zhang, Z.F. Lin, D.Q. Yin, H.Q. Tang, *Environ. Sci. Technol.* 47 (2013) 518–525.
- [20] J. Xu, L.S. Tan, S.A. Baig, D.L. Wu, X.S. Lv, X.H. Xu, *Chem. Eng. J.* 231 (2013) 26–35.
- [21] L.J. Xu, J.L. Wang, *J. Hazard. Mater.* 186 (2011) 256–264.
- [22] S. Luo, S.G. Yang, Y.G. Xue, F. Liang, C. Sun, *J. Hazard. Mater.* 192 (2011) 1795–1803.
- [23] Z.R. Lin, X.H. Maa, L. Zhao, Y.H. Dong, *Chemosphere* 101 (2014) 15–20.
- [24] Y.J. Wu, J.H. Zhang, Y.F. Tong, X.H. Xu, *J. Hazard. Mater.* 172 (2009) 1640–1645.
- [25] L. Li, M.H. Fan, R. Brown, J.H. Van Leeuwen, J.J. Wang, W.H. Wang, *Crit. Rev. Environ. Sci. Technol.* 36 (2006) 405–431.
- [26] R.X. Huang, Z.Q. Fang, X.M. Yan, W. Cheng, *Chem. Eng. J.* 197 (2012) 242–249.
- [27] Z.Q. Fang, X.H. Qiu, J.H. Chen, X.Q. Qiu, *Desalination* 267 (2011) 34–41.
- [28] Y.H. Peng, M.K. Chen, Y.H. Shih, *J. Hazard. Mater.* 260 (2013) 844–850.
- [29] Y.Y. Xie, Z.Q. Fang, W. Cheng, P.E. Tsang, D.Y. Zhao, *Sci. Total Environ.* (2014), 485–486, 363–370.
- [30] Y.L. Zhang, C.S. Han, G.H. Zhang, D.D. Dionysiou, M.N. Nadagouda, *Chem. Eng. J.* 268 (2015) 170–179.
- [31] Q. Xiao, Z.C. Si, J. Zhang, C. Xiao, X.K. Tan, *J. Hazard. Mater.* 150 (2008) 62.
- [32] N.N. Wang, T. Zheng, J.P. Jiang, P. Wang, *Chem. Eng. J.* 260 (2015) 386–392.
- [33] J.G. Yu, W.G. Wang, B. Cheng, B.L. Su, *J. Phys. Chem. C* 113 (2009) 6743–6750.
- [34] J.E. Martin, A.A. Herzing, W.L. Yan, X.Q. Li, B.E. Koel, C.J. Kiely, W.X. Zhang, *Langmuir* 24 (2008) 4329–4334.
- [35] W.L. Yan, A.A. Herzing, C.J. Kiely, W.X. Zhang, *J. Contam. Hydrol.* 118 (2010) 96–104.
- [36] X.S. Lv, J. Xu, G.M. Jiang, J. Tang, X.H. Xu, *J. Colloid Interface Sci.* 369 (1) (2012) 460–469.
- [37] D. Li, D.L. Jiang, M. Chen, J.M. Xie, Y.Y. Wu, S.C. Dang, J.X. Zhang, *Mater. Lett.* 64 (22) (2010) 2462–2464.
- [38] A.H. Lv, C. Hu, Y.L. Nie, J.H. Qu, *Appl. Catal. B Environ.* (2012), 117–118, 246–252.
- [39] X.B. Hu, B.Z. Liu, Y.H. Deng, H.Z. Chen, S. Luo, C. Sun, Po Yang, S.G. Yang, *Appl. Catal. B Environ.* 107 (2011) 274–283.
- [40] H. Zhang, J.H. Zhang, C.Y. Zhang, *Ultrason. Sonochem.* 16 (3) (2009) 325–330.
- [41] L.J. Xu, J.L. Wang, *Environ. Sci. Technol.* 46 (2012) 10145–10153.
- [42] Y. H. Shih, Y.T. Tai, *Chemosphere* 78 (2010) 1200–1206.
- [43] T.C.H. An, L. Zu, G.Y. Li, S.H.G. Wan, B.X. Mai, P.K. Wong, *Bioresour. Technol.* 102 (2011) 9148–9154.
- [44] G.J. Su, H.J. Lu, L.X. Zhang, A.Q. Zhang, L.Y. Huang, S. Liu, L.W. Li, M.H. Zheng, *Environ. Sci. Technol.* 48 (2014) 6899–6908.
- [45] L.Y. Huang, G.J. Su, A.Q. Zhang, Y.L. Shi, C.B. Xia, H.J. Lu, L.W. Li, S. Liu, M.H. Zheng, *J. Hazard. Mater.* 261 (2013) 451–462.
- [46] J. Lichtenberger, M.D. Amiridis, *J. Catal.* 223 (2) (2004) 296–308.
- [47] Y. Zhuang, S.W. Ahn, A.L. Seyfferth, Y.M. Slowey, S. Fendorf, R.G. Luthy, *Environ. Sci. Technol.* 45 (2011) 4896–4903.
- [48] K. Yoshioka, E. Sakai, M. Daimon, *J. Am. Cream. Soc.* 80 (10) (1997) 2667–2671.
- [49] L.J. Xua, J.L. Wang, *Appl. Catal. B Environ.* (2012), 123–124, 117–126.
- [50] N. Wang, L.H. Zhu, D.L. Wang, M.Q. Wang, Z.F. Lin, H.Q. Tang, *Ultrason. Sonochem.* 17 (2010) 526–533.
- [51] X.Y. Zhang, Y.B. Ding, H.Q. Tang, X.Y. Han, L.H. Zhu, N. Wang, *Chem. Eng. J.* 236 (2014) 251–262.
- [52] M.L. Wang, G.D. Fang, P. Liu, D.M. Zhou, C. Ma, D.J. Zhang, J.H. Zhan, *Appl. Catal. B Environ.* 188 (2016) 113–122.
- [53] Y.X. Wang, H.Q. Sun, X.G. Duan, H.M. Ang, M.O. Tadé, S.B. Wang, *Appl. Catal. B Environ.* (2015), 172–173, 73–81.
- [54] G.D. Fang, D.D. Dionysiou, Y. Wang, S.R. Al-Abedc, D.M. Zhou, *J. Hazard. Mater.* (2012), 227–228, 394–401.